JACS
JOURNAL OF THE AMERICAN CHEMICAL SOCIETY

Article

pubs.acs.org/JACS

In Situ AFM Imaging of Li−O_2 Electrochemical Reaction on Highly Oriented Pyrolytic Graphite with Ether-Based Electrolyte

Rui Wen,[†] Misun Hong,[†,‡] and Hye Ryung Byon*[,†]

[†]Byon Initiative Research Unit (IRU), RIKEN, Hirosawa 2-1, Wako, Saitama 351-0198, Japan

[‡]Department of Chemistry, Pohang University of Science and Technology (POSTECH), San 31, Hyoja-Dong, Nam-Gu, Pohang 790-784, South Korea

Supporting Information

ABSTRACT: Understanding the lithium−oxygen (Li−O_2) electrochemical reaction is of importance to improve reaction kinetics, efficiency, and mitigate parasitic reactions, which links to the strategy of enhanced Li−O_2 battery performance. Many in situ and ex situ analyses have been reported to address chemical species of reduction intermediate and products, whereas details of the dynamic Li−O_2 reaction have not as yet been fully unraveled. For this purpose, visual imaging can provide straightforward evidence, formation and decomposition of products, during the Li−O_2 electrochemical reaction. Here, we present real-time and in situ views of the Li−O_2 reaction using electrochemical atomic force microscopy (EC-AFM). Details of the reaction process can be observed at nano-/micrometer scale on a highly oriented pyrolytic graphite (HOPG) electrode with lithium ion-containing tetraglyme, representative of the carbon cathode and ether-based electrolyte extensively employed in the Li−O_2 battery. Upon oxygen reduction reaction (ORR), rapid growth of nanoplates, having axial diameter of hundreds of nanometers, length of micrometers, and ∼5 nm thickness, at a step edge of HOPG can be observed, which eventually forms a lithium peroxide (Li_2O_2) film. This Li_2O_2 film is decomposed during the oxygen evolution reaction (OER), for which the decomposition potential is related to a thickness. There is no evidence of byproduct analyzed by X-ray photoelectron spectroscopy (XPS) after first reduction and oxidation reaction. However, further cycles provide unintended products such as lithium carbonate (Li_2CO_3), lithium acetate, and fluorine-related species with irregular morphology due to the degradation of HOPG electrode, tetraglyme, and lithium salt. These observations provide the first visualization of Li−O_2 reaction process and morphological information of Li_2O_2, which can allow one to build strategies to prepare the optimum conditions for the Li−O_2 battery.

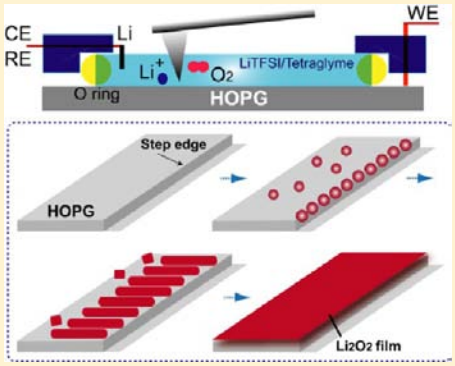

INTRODUCTION

A nonaqueous Li−O_2 battery has a promising theoretical specific energy density (∼3 kWh kg^{-1}) to achieve performance for a long-range driving electric vehicle (EV). Much attention has been given to create a rechargeable Li−O_2 battery, which, however, presently suffers from the great challenges of poor cycling stability and huge cathodic polarization.[1−5] Mitigating performance degradation has been impeded so far. This is mostly due to a lack of understanding of the electrochemical reactions involved in the operation of a Li−O_2 cell.[3,6,7] Ex situ analysis has indicated that the ideal Li−O_2 electrochemical reaction ($2Li^+ + O_2(g) + 2e^- \leftrightarrow Li_2O_2(s)$) is not the sole reaction occurring in the Li−O_2 cell but is accompanied by parasitic reactions with respect to the stability of nonaqueous electrolyte and lithium salt. It has been evidenced by the presence of Li_2CO_3 and lithium carboxylate species along with Li_2O_2 after the reduction reaction.[8−10] Further efforts have been devoted to reveal the actual Li−O_2 chemical and electrochemical reactions in the Li−O_2 cell using various analytical techniques.[11−18] However, ex situ probes have delivered fragmentary information, and as a result many hypotheses have been proposed, which complicate the details of the reaction mechanism. Recently, in situ probes such as Raman microscopy,[19] differential electrochemical mass spectrometry (DEMS),[20−25] ambient pressure XPS,[26] and X-ray diffraction (XRD)[27] have revealed evidence of the potential-dependent electrochemical reaction during the operation of the Li−O_2 cell, demonstrating the working mechanism of Li−O_2 cells at different conditions. However, full details of the dynamic Li−O_2 reaction have not as yet been unraveled despite many endeavors.[7,24,28−30] One of the solutions to understand the Li−O_2 electrochemical reaction is a closer look of the total reaction process using imaging tools because the visualization provides straightforward evidence for the formation/decomposition of reaction products. Furthermore, the visual monitoring of reaction products enables the investigation of the correlation between product morphology and chemical species during the Li−O_2 reaction. This study reveals the nucleation site of the product on the conductive electrode, contact area, and product size and shape, which can provide the morphological information correlating with sluggish reaction

Received: May 23, 2013
Published: June 28, 2013

   dx.doi.org/10.1021/ja405188g | J. Am. Chem. Soc. 2013, 135, 10870−10876

and poor reversibility in the current Li−O_2 battery. For this purpose, the use of AFM with a wide range of spatial resolutions from nano- to micrometer is appropriate to observe a series of nucleation, growth, and decomposition from various products. In addition, a potentiostat/galvanostat coupled with the AFM (EC-AFM) can offer conditions almost identical to those of the actual Li−O_2 cell during in situ observation.

Here, we present real-time and in situ imaging of the Li−O_2 electrochemical reaction using EC-AFM for the first time. The model Li−O_2 cell coupled with EC-AFM displays a reversible Li−O_2 reaction for the first cycle based on HOPG electrode with ether-based electrolyte. A typical Li_2O_2 product formed dominantly during the reduction reaction has a nanoplate shape having axial diameter of hundreds of nanometers, length of micrometers, and ∼5 nm thickness. The Li_2O_2 nanoplates are grown from step edges of HOPG rapidly and make a film. Upon the oxidation, the elimination of Li_2O_2 can be observed. A thick Li_2O_2 film delays its complete decomposition, which demands high potential. These observations demonstrate that the dynamic reaction to form and decompose Li_2O_2 can be scrutinized in a model Li−O_2 cell using EC-AFM.

EXPERIMENTAL SECTION

Preparation of Li−O_2 Cell. The Li−O_2 cell was composed of HOPG substrate as the working electrode (WE), Li wire as the counter and reference electrodes (CE and RE), and an O_2 gas-saturated tetraethylene glycol dimethyl ether (tetraglyme, UBE, <20 ppm of H_2O) containing 0.5 M of lithium bis(trifluoromethanesulfonyl)imide (LiTFSI, Kanto Chemical Co.) as the nonaqueous electrolyte (Figure S1). HOPG (2 cm (w) × 2 cm (d) × 0.1 cm (t), SPI-II grade, SPI, U.S.) substrate was heat-treated at 60 °C for 2 days under vacuum, and then the uppermost layers were carefully cleaved by adhesive tape before use. The clean HOPG substrate was positioned on the Li−O_2 cell, and the HOPG surface was connected with a gold-coated wire. 0.9 mL of tetraglyme containing Li salt was then added to Li−O_2 cell and bubbled with dried O_2 (Tomoe Shokai Co., Ltd., >99.999%) or argon (Ar) gas (99.9999%) over 30 min in a dry Ar-filled glovebox. Li metal (Acros Organics, 99+%) suspended from a platinum wire was then immersed in the electrolyte. It is noted that Li wire should be suspended along the inner wall of Li−O_2 cell to avoid contact with the scanner nose-cones. The distance between the HOPG and Li metal was ∼2 mm. Li wire fully soaked in the electrolyte was appreciably stable, maintaining a metallic lustrous surface and silver color during experiment, probably due to a protective layer formed on the Li surface.[24]

Electrochemical Performance and Image Scanning Using EC-AFM. Electrochemical performance testing was carried out using a potentiostat/galvanostat coupled with the AFM (EC-AFM, Agilent 5500 AFM/SPM) in an Ar-filled glovebox. All potentials were referred to Li^+/Li. Cyclic voltammetry (CV) curves were recorded in the range 2.0−4.5 V (or 1.5−4.5 V) at a sweep rate of 5 mV s^{-1} using EC-AFM and other potentiostat (WPG 100e, WonATech) for the confirmation. The potential was swept toward negative potential (from open circuit potential (OCP) to 2.0 V) for the reduction and positive (2.0 to 4.5 V) for the oxidation reaction. To obtain a thick reduction product film, the potential was kept at 2.0 V for 1 h before the oxidation process. A galvanostatic measurement was performed at a current rate of 1.57 μA cm^{-2} under the same conditions and using the same Li−O_2 cell. The HOPG surface was scanned by EC-AFM using an insulating triangular silicon nitride AFM tip (radius <10 nm, force constant of 0.08 N m^{-1}, Olympus) during electrochemical examination (contact mode providing topography and deflection images, imaging in Li−O_2 cell containing the liquid electrolyte), or using a silicon tip (radius <7 nm, force constant of 42 N m^{-1}, 330 kHz of frequency, Agilent) after the examination (tapping mode providing topography and phase images, imaging in Ar gas (out of Li−O_2 cell)). For tapping mode imaging, HOPG electrodes were dissembled from the Li−O_2 cell, washed out by anhydrous dimethyl carbonate (DMC, Chameleon Reagent, <10 ppm of H_2O) solvent several times, and dried in a vacuum chamber at 60 °C for 2 h. All experiments were carried out in an Ar-filled glovebox to avoid air contamination.

Characterization. XPS analysis was performed on a VG ESCALAB 250 spectrometer (Thermo Fisher Scientific K.K.) with monochromatic Al Kα X-ray radiation at 15 kV and 200 W. The base pressure of the XPS chamber was less than 10^{-8} Pa. X-ray photoelectron spectra of 1-cycled reduction and oxidation electrodes were obtained by discharge to 2.0 V and recharge up to 4.5 V, respectively. The 5-cycled electrodes were obtained by sweeping toward negative potential to 2.0 V and positive potential up to 4.5 V at a sweeping rate of 5 mV s^{-1}, respectively, using the potentiostatic method. After being washed and dried, electrodes were conveyed in Ar-filled hermetic containers. All spectra on HOPG electrode were calibrated by setting the C 1s photoemission peak for sp^2-hybridized carbon to 284.3 eV.

RESULTS AND DISCUSSION

Cyclic Voltammetry Curves of Li−O_2 Cell with Ether-Based Electrolyte. CVs coupled with AFM scanning were performed in the Ar-filled glovebox to investigate ORR and OER potentials on the Li−O_2 electrochemical cell that was composed of HOPG and Li metal electrodes with an O_2 gas-saturated tetraglyme electrolyte containing 0.5 M of LiTFSI (see Experimental Section and Figure S1). The HOPG, composed of atomically flat, high crystallinity, and low surface area carbon, enables the probing of the dynamic reactions perceptibly with uniform wettability and O_2 diffusivity. The tetraglyme has suitable stability for the superoxide radical ($O_2^{\bullet-}$) as a reduction form of O_2 and low volatility,[9,31,32] which is requisite for investigation of the Li−O_2 electrochemical reaction on the initial cycles, in an open Li−O_2 cell.

Figure 1a show CV curves in 2.0−4.5 V at a sweep rate of 5 mV s^{-1} in Ar and O_2 gas. The CV curve measured under O_2

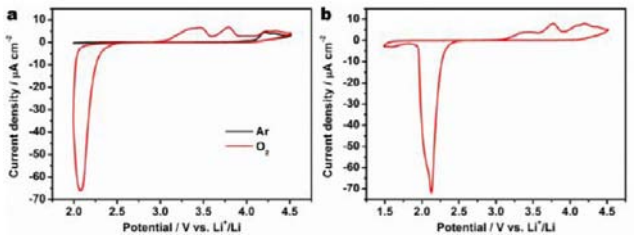

Figure 1. Representative CV curves in Li−O_2 cells with 0.5 M LiTFSI in tetraglyme at a sweep rate of 5 mV s^{-1}. The red and black curves are under O_2 and Ar gas, respectively. The potential ranges are (a) 2.0−4.5 V and (b) 1.5−4.5 V.

shows the onset reduction potential at ∼2.5 V (referenced to Li^+/Li), which is sharply increased from 2.3 V and approaches to a maximum at 2.1−2.2 V as evidenced by the wider potential scan range in 1.5−4.5 V in Figure 1b. The oxidation curve displays oxygen evolution peak currents at 3.4−3.5 and 3.8 V, which are not observed under Ar. Over 4.0 V, broad peak currents appear in 4.2−4.4 V under both O_2 and Ar, which are attributed to the oxidation of HOPG surface (Figure S2 for Raman spectra) and tetraglyme electrolyte catalyzed by HOPG.[29] Upon ORR, the O_2 gas is reduced to $O_2^{\bullet-}$ from the conducting electrode surface ($O_2(g) + e^- \rightarrow O_2^{\bullet-}$), which then reacts with abundant Li^+ ions in the electrolyte ($Li^+ + O_2^{\bullet-} \rightarrow LiO_2$, then (1) $2LiO_2 \rightarrow Li_2O_2 + O_2$[19,28,33,34] or (2) $LiO_2 + Li^+ + e^- \rightarrow Li_2O_2$[20,21,24,27,34]). As a result, Li_2O_2 is formed on the electrode (total reaction equation: $2Li^+ + O_2(g)$

dx.doi.org/10.1021/ja405188g | J. Am. Chem. Soc. 2013, 135, 10870−10876

+ $2e^- \rightarrow Li_2O_2(s)$). The Li_2O_2 can be decomposed upon OER ($Li_2O_2(s) \rightarrow 2Li^+ + O_2(g) + 2e^-$). During ORR, the HOPG electrode exhibits negatively shifted onset and peak-current potentials as compared to those of glassy carbon and other carbon electrodes, although the lithium salt concentration and sweeping rates are not identical.[24,29,35] This probably arises from the high crystallinity of HOPG with less defective sites and functional groups, that is, less nucleation sites for Li_2O_2.[36,37]

In Situ AFM Imaging for Oxygen Reduction Reaction Process. To observe the real-time ORR process in the initial stage, we monitored the clean HOPG surface in the Li−O_2 cell using EC-AFM. In situ images were acquired at 2.4, 2.2, 2.1, and 2.0 V along the CV trace via negative-direction sweep, which corresponded to Figure 2a−d. The potential was held at each point for 6.5 min during the image scan. Just after the onset of ORR (2.4 V), atomically flat terrace (T) and step edges (S_1−S_3) are visible on the bare HOPG, while no obvious reduction product is observed at nanometer scale (Figure 2a). When the potential approaches 2.2 V, nanoparticles (NPs, diameter (d) = 3−10 nm, measured from the height profile) form along the step edges of HOPG (S_1 and S_3) (Figure 2b).

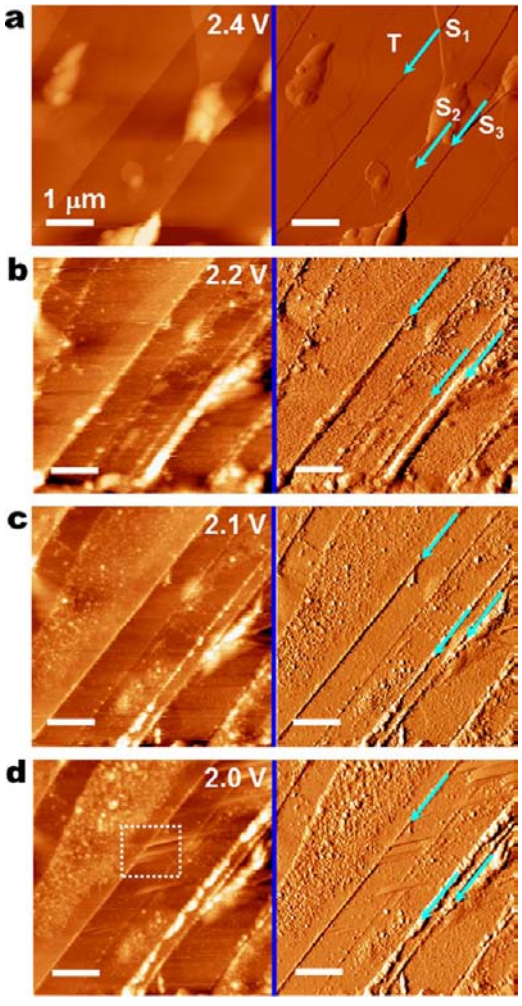

Figure 2. In situ AFM images of HOPG electrode upon ORR in a Li−O_2 cell with 0.5 M LiTFSI in tetraglyme. (a−d) Topography (left) and deflection (right) images at 2.4, 2.2, 2.1, and 2.0 V. The scale bars are 1 μm.

These NPs then disappear but manifestly emerge on the terrace at 2.1 V (d = 5−15 nm, Figure 2c). When the potential is close to 2.0 V (Figure 2d), the NPs on the terrace become larger (d = 8−25 nm), while new NPs are also created along the previously unoccupied step edge (S_2). Moreover, the elongated products indicated by the dashed box become visible.

We focused on the growth of the elongated products, that is, rectangular nanoplates, further. Hereafter we define the various nano-sized morphologies, all sharing the same height (∼5 nm, see below), as nanoplates. In situ AFM images were acquired under the time-dependent reaction process at 2.0 V, shown in Figure 3a−e with 6.5 min scan time per image. Figure 3a is a high-magnification image of the indicated region in Figure 2d, exhibiting the NPs on the terrace and the rectangular nanoplates (axial diameter of 500 nm and length of micron scale) at the step edge of HOPG that was indicated by the dashed line in the deflection image. Some nanoplates are perpendicularly grown from the step edge during the image scanning, resulting in unclear contours due to rapid growth. Figure 3b−e focuses on the edge sides of nanoplates that are slightly shifted and somewhat larger during the scanning due to the broadening of tip convolution. In this series of images, we can observe three features: NPs on terrace (1), NP arrays close proximity to steps of the nanoplate (2), and a nanoplate (3). Simply, the large NPs (1) and the NP arrays (2) gradually disperse and migrate (2′ in Figure 3e), while the nanoplate (3′) is rapidly grown as shown in Figure 3e. These nanoplates consist of nanostructural particles (dashed box in Figure 3c and its high-magnification image in Figure S3a), which are smaller than the NPs (1) and NP arrays (2) and have a nanoscopically

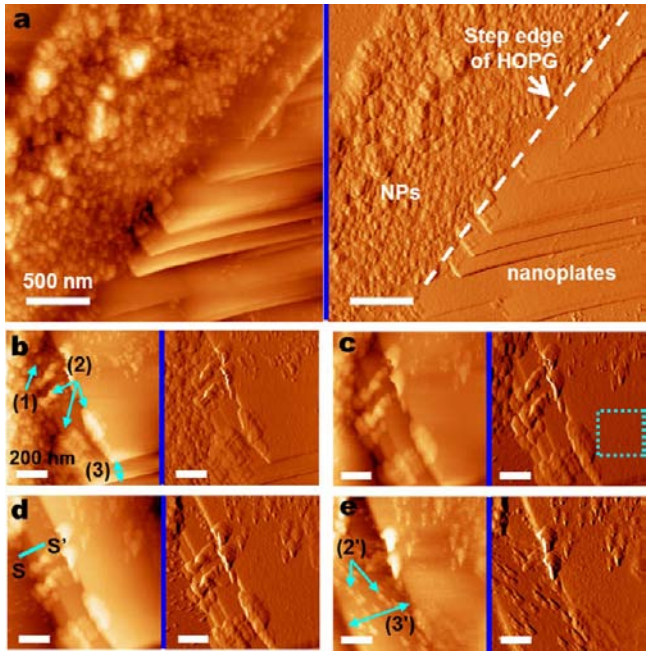

Figure 3. Time-dependent AFM images of HOPG electrode during ORR in Li−O_2 cells at 2.0 V. (a−e) Topography (left) and deflection (right) images with 6.5 min scan time per image. (a) is the high-magnification image of the dashed box region from Figure 2d. The scale bars in (a) are 500 nm. The (1), (2), and (3) in (b) indicated by the arrows represent NPs on terrace, NP arrays close to steps of the nanoplates, and rectangular nanoplates. (2′) and (3′) in (e) are dispersed NPs from separated NP arrays and a grown nanoplate, respectively. The scale bars in (b)−(e) are 200 nm.

dx.doi.org/10.1021/ja405188g | J. Am. Chem. Soc. 2013, 135, 10870−10876

uniform height. The thickness of the nanoplate indicated by S−S′ in Figures 3d is ∼5 nm, as shown in Figure S3b.

These observations provide insight of the dynamic ORR process in the Li−O_2 cell at the initial stage. Most of the NPs nucleate along the step edge of HOPG, at the beginning of reduction sweeping (shown schematically in Figure 4a(1),(2)),

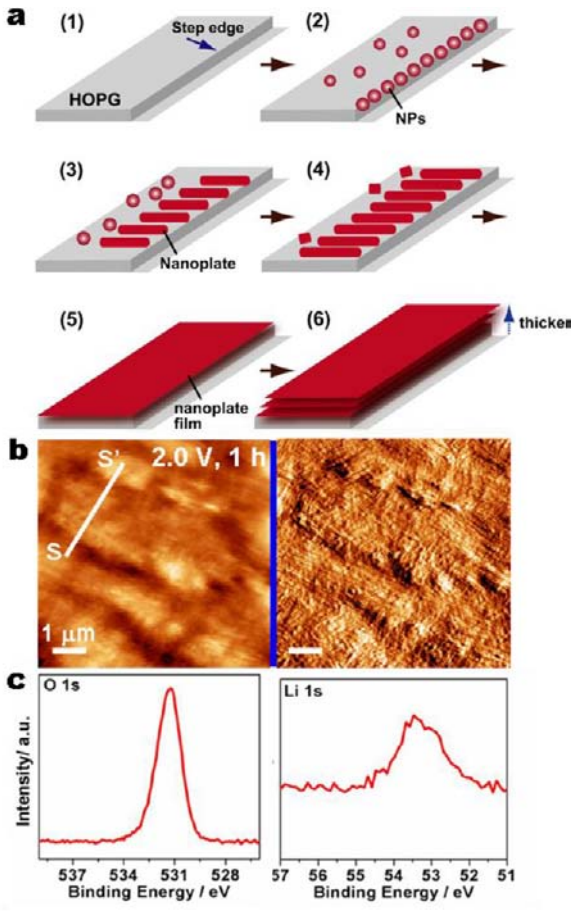

Figure 4. Li_2O_2 film after ORR on HOPG. (a) Schematic illustration of ORR process. (b) Topography (left) and deflection (right) AFM images of nanoplate film acquired at 2.0 V for 1 h holding using the potentiostatic method. The scale bars are 1 μm. (c) XPS of nanoplate film in O and Li 1s BE regions.

due to its high surface energy and abundant active reaction sites.[38] These NPs can be the starting substance for growth of the nanoplate or incorporated into the growing nanoplate during ORR (Figure 4a(3)−(4)). In Figure 2, some of the NPs, becoming larger, migrate to the terrace. These NPs then agglomerate and disperse under the initial reduction process (Figure 3). We suggest that these large NPs can eventually be slowly incorporated into a nanoplate film or form large agglomerated particles upon further ORR (Figure 4a(4)) because they are not found easily after deep reduction (Figure 4b). Unlike these NPs, the stable nanoplates, mostly formed at the step edge of HOPG where the NPs can be nucleated, grow swiftly perpendicular to the HOPG step edge (Figure 4a(3)) (Figure 3). Prolonged reduction produces more nanoplates that cover the entire HOPG surface immediately and become thicker (Figure 4a(5),(6)). Figure 4b shows a film uniformly covering the HOPG surface, acquired at 2.0 V for 1 h. This film surface consists of abundant nanoplates, which have a rod shape. Many rod-shaped nanoplates are deposited with diverse orientations on the film surface. Individual nanoplates had an average axial diameter of 50 nm, length of 0.8 μm, and step height of ∼5 nm (S−S′ in Figure 4b and its height profile in Figure S4). The step height of film is identical to that for a rectangle-shaped nanoplate formed at the initial stage (Figure S3b). This unique height of the nanoplates is probably related to the limited charge transport to form Li_2O_2 with low electronic conductivity via the tunneling current.[39] This film is identifed as Li_2O_2 by the X-ray photoelectron spectra. Figure 4c shows the O 1s and Li 1s peak at ∼531.3 and ∼53.4 eV of binding energy (BE), respectively. This O 1s peak is assigned to the Li−O bond in Li_2O_2,[26] which is in good agreement with the reference powder of Li_2O_2 (Figure S5).

Similar Li_2O_2 nanoplate and film morphologies are also observed using a galvanostatic method. The discharge process was performed at a current rate of 1.57 μA cm^{-2} in the same Li−O_2 cell. A representative discharge curve in Figure 5a shows

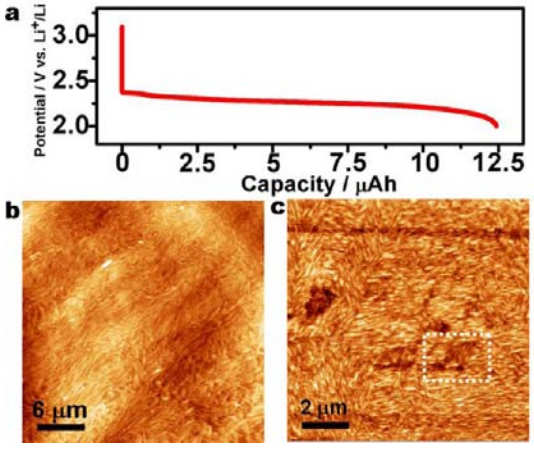

Figure 5. Discharge curve and topography images of Li_2O_2 film acquired via the galvanostatic method. (a) Representative discharge curve at a current rate of 1.57 μA cm^{-2} and nanoplate films acquired at (a) 2.2 and (b) 2.0 V.

∼2.3 V of onset potential of discharge, which is gradually decreased as the Li_2O_2 film is formed. Figure 5b shows the Li_2O_2 nanoplates uniformly and thinly formed on the HOPG at 2.2 V with an average axial diameter of 100 nm and length of 1.5 μm. The lateral sizes of rod-shaped nanoplates are different from the ones formed via the potentiostatic method. Nevertheless, it is noteworthy that the aspect ratios of both nanoplates are similar. Further discharge at 2.0 V (a capacity of ∼12.5 μAh, total 4 h) resulted in a denser and thicker Li_2O_2 film (Figure 5c). The topmost surface of Li_2O_2 film is composed of smaller nanoplates (average axial diameter of 18 nm and length of 80 nm). In addition, the local film surface with the absence of Li_2O_2 nanoplates indicated by the dashed box in Figure 5c reveals the under-layered nanoplates having similar shape but different orientation (Figure S6). This incomplete film surface and smaller size of rod-shaped nanoplates indicate that the new layer of Li_2O_2 can be formed from the Li_2O_2 film surface. We suggest that the growth on the top surface of Li_2O_2 can take place by (1) $O_2^{\bullet-}$ transported via electrolyte after the O_2 gas reduction on the remaining bare surface of HOPG or (2) charge transport through the defects of Li_2O_2 or boundaries in between Li_2O_2 nanoplates. Because of the very limited area of the HOPG surface exposed during

dx.doi.org/10.1021/ja405188g | J. Am. Chem. Soc. 2013, 135, 10870−10876

ORR and low electronic conductivity of Li_2O_2, the Li_2O_2 growth on the top surface of Li_2O_2 is slow, and the resultant Li_2O_2 nanoplates have smaller size.

Such a unique Li_2O_2 nanoplate morphology is only acquired from O_2 gas saturated ether-based electrolyte. There is no Li_2O_2 nanoplate morphology in the Ar gas-bubbled tetraglyme electrolyte (Figure S7). When the O_2-saturated carbonate electrolyte is employed, which has been known to produce Li_2CO_3 due to the degradation of electrolyte,[8] a formless ORR product is observed (Figures S8,9).

In Situ AFM Imaging for Oxygen Evolution Reaction Process. The Li_2O_2 nanoplates obtained by discharge at 2.2 V were then oxidized via positive-direction sweep at a sweeping rate of 5 mV s^{-1}. The OER process starts from ~3.1 V and is vigorous in the range 3.3−4.0 V (Figure 1a). The corresponding images of Li_2O_2 decomposition in Figure 6a−c

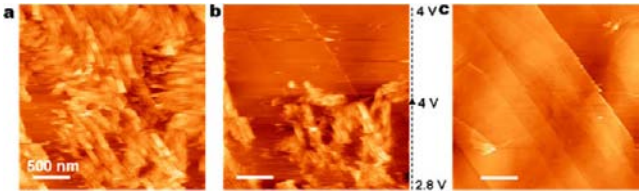

Figure 6. In situ and sequantial AFM topography images of Li_2O_2 nanoplates on HOPG upon OER in Li−O_2 cell. (a) Li_2O_2 nanoplates acquired via the galvanostatic discharge at a cutoff potential of 2.2 V. (b) Potential-dependent view of HOPG electrode from 2.8 (bottom) to 4.0 V (middle to top) at a sweeping rate of 5 mV s^{-1}. (c) Clean HOPG electrode at 4.0 V. The scale bars are 500 nm.

exhibit elimination of the nanoplates in the potential range of 2.8−4.0 V. In particular, the swift and complete decomposition of Li_2O_2 nanoplates is observed in the range 3.9−4.0 V, and no product remained at 4.0 V.

The denser and thicker Li_2O_2 film acquired by the deep ORR (1 h at 2.0 V) via the potentiostatic method, however, remains over 4.0 V. There is no morphological change on the Li_2O_2 film surface up to 4.38 V (Figure 7a−d). This incomplete decomposition is probably due to the thick Li_2O_2 with low electronic conductivity, which can incur high over-potential during OER (Figure S10 for linear sweep voltammetry (LSV)). Further maintaining the potential at 4.38 V with 8.5 min of a scan time per image then allows its dynamic decomposition. Upon the initial period at 4.38 V, the surface morphology is slightly altered around the topographically highest domain indicated by the arrow in Figure 7e. Following that, rapid depletion occurs in the whole Li_2O_2 film surface, which is sufficiently rapid to prevent a clear visible image capture (Figure 7f,g). The Li_2O_2 film becomes thinner and eventually completely depleted as evidenced by the appearance of the step edges of HOPG in Figure 7g. The terraces and step edges on HOPG are visibly exposed at 4.5 V (Figure 7h), and there is no residual product. This delayed and abrupt elimination of Li_2O_2 film surface implies that the decomposition process of the Li_2O_2 film is initiated from the bottom, which cannot be detected from the top surface images despite performing OER. It turns out that the OER process primarily occurs at the interface of HOPG/Li_2O_2, providing the most favorable route to release and transport the electrons from Li_2O_2 to HOPG.[19,24]

The Li_2O_2 film is completely decomposed at 4.5 V, determined from no Li peak on the electrode in XPS (Figure

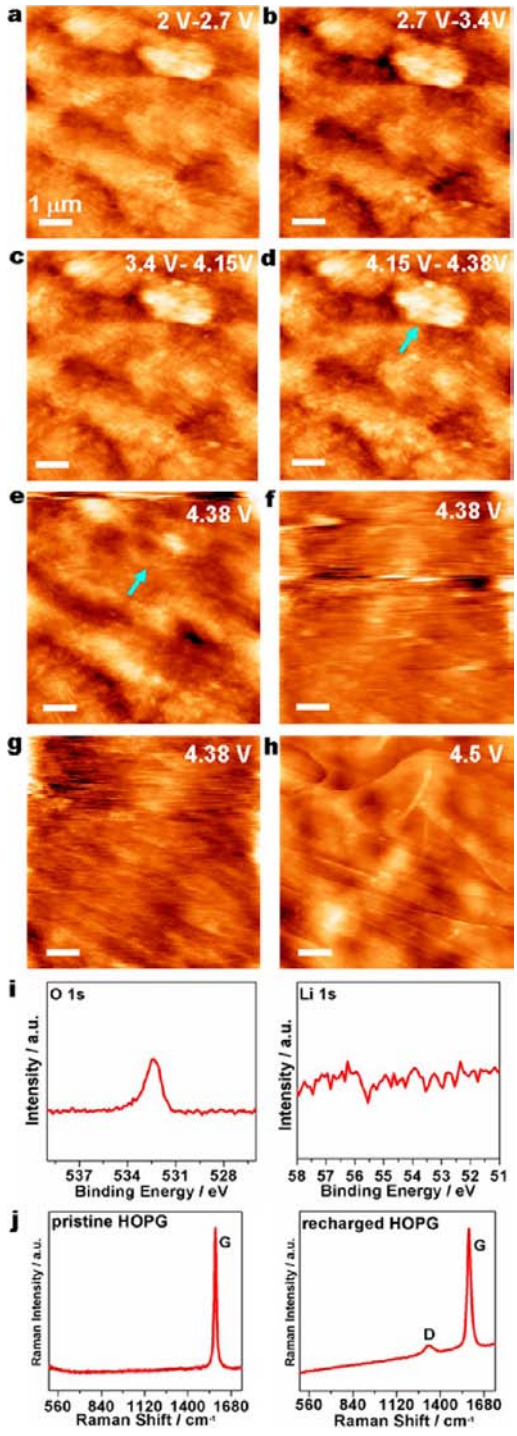

Figure 7. In situ AFM images of thick Li_2O_2 film on HOPG during OER in Li−O_2 cell, XPS, and Raman analysis. (a−f) Topography images of Li_2O_2 film at (a) 2.0−2.7, (b) 2.7−3.4, (c) 3.4−4.15, (d) 4.15−4.38, (e−g) 4.38, and (h) 4.5 V obtained sequentially. The scale bars are 1 μm. (i) XPS in O (left) and Li (right) 1s BE regions. (j) Raman spectra of pristine HOPG (left) and HOPG after OER (right).

7i). A small O 1s peak at 532.2 eV is accordingly attributed to the slightly oxidized carbon from HOPG supported by the appearance of a D band in the Raman spectrum (Figure 7j). This oxidation of carbon electrode has been also reported in Li−O_2 cells charging at a potential above 3.5 V[40] and under Ar (Figure S2). The impurity from TFSI in the Li salt is also found in the F 1s BE region (Figure S11).

dx.doi.org/10.1021/ja405188g | J. Am. Chem. Soc. 2013, 135, 10870−10876

AFM Images of 5-Cycled Electrodes. Further cycles were also investigated to explore the reversibility of the Li−O_2 reaction. Figure S12 and Figure 8a,b show 5-cycled CV,

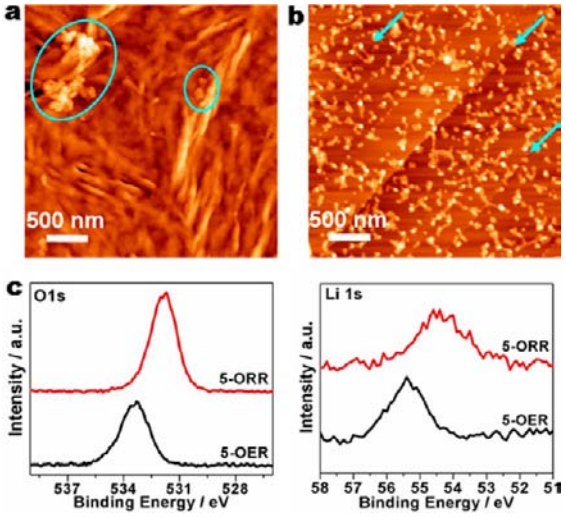

Figure 8. The 5-cycled AFM images of HOPG electrode and XPS analysis. (a,b) Topography images after (a) 5-cycled ORR and (b) 5-cycled OER electrodes. The electrodes were washed and dried before scanning. (c) X-ray photoelectron spectra of 5-cycled ORR (5-ORR) and 5-cycled OER (5−OER) in O (left) and Li (right) 1s BE regions.

ORR, and OER products on HOPG, respectively. The CV curves swept in the 2.0−4.5 V range of potential for five cycles at a sweeping rate of 5 mV s^{-1} show gradual decrease in reduction and oxidation peak-currents on cycling. The cycled HOPG electrode was washed out, dried, and scanned via the tapping mode under Ar gas (out of Li−O_2 cell) in the glovebox. The 5-cycled ORR electrode in 2.0−4.5 V shows sparse products, mixing with the elongated product and aggregated particular forms indicated by the circles in Figure 8a. These morphologies are somewhat different from the Li_2O_2 structures observed after the first ORR (Figure 2). The elongated products seem to have a shapeless and rough surface with variable lengths. XPS in Figure 8c reveals the O 1s peak at ∼531.8 eV of the peak center arising from the combination of Li_2O_2 and Li_2CO_3 (∼532 eV).[22,40,41] This suggests that the ORR product morphology can be disrupted by the formless Li_2CO_3 (Figures S8,9). On the 5-cycled OER electrode, many nanoparticulate products having an average diameter of 20 nm still remain as shown in Figure 8b. This particulate form of byproducts is dispersed along the step edges (arrows) and on the terraces. XPS exhibits further shifted O 1s (∼533.2 eV) and Li 1s (∼55.4 eV) peaks, which are not overlapped with Li_2O_2 peaks. These byproducts involve Li_2CO_3 and lithium acetate (∼533.7 eV for the O 1s peak) as compared to the corresponding reference powders (Figure S5).[12] In addition, the 5-cycled OER electrode contains a large quantity of deteriorated TFSI evidenced by the presence of two large F 1s peaks (∼686.2 and 689.8 eV) that are not shown after the first cycle (Figure S11). These byproducts produced by the degradation of tetraglyme electrolyte, Li salt, and HOPG carbon in Li−O_2 cell[9,12,40,42] can be deposited on the HOPG surface on cycling, which possibly hinders the formation of Li_2O_2 on the electrode surface by blocking the nucleation sites and increasing the interface resistance.[22,40] It demonstrates that the Li−O_2 reaction efficiency decreases during the initial several cycles in the current Li−O_2 cell as byproducts are coprecipitated with the Li_2O_2 on the electrode as also shown by time-of-flight secondary ion mass spectrometry (ToF-SIMS) studies.[42] Further study to measure the increasing byproduct ratio per cycle using various analytical tools[43] will aid in understanding the role of accumulated byproducts with respect to the cyclic performance.

In addition to the full ORR and OER potential range, we also observed 5-cycled HOPG electrodes in the limited potential range at 2.2−4.2 V, which allows the formation of Li_2O_2 (Figure 2) and avoids the oxidation of tetraglyme electrolyte (Figure 1). The CV curves in Figure S13 show small OER peaks at 3.3, 3.5, and 4.0 V with uprising current over 4.0 V and gradually decreased ORR currents during five cycles. The AFM image of 5-cycled OER electrode depicts the mixture of nanoplates and nanoparticles with high density, which implies incomplete decomposition of Li_2O_2 and byproducts.[9,22,23] Consequently, the restricted potential range is not beneficial in terms of attenuating the deposition of byproducts for cyclings. It is noteworthy that the reaction conditions such as carbon material, electrode structure, catalyst, concentration of lithium salt, sweeping rate, potential range, measurement method, and cell design are different from some earlier reports,[13,29,32,44] which can result in different conclusions for the cyclic performance in the limited ORR and OER potential range.

■ CONCLUSION

In summary, we showed the first visual evidence of real-time and in situ Li−O_2 electrochemical reaction process in the Li−O_2 model cell coupled with EC-AFM. We demonstrated the growth of Li_2O_2 film from NPs and nanoplate morphologies. The NPs, formed on the step edges of the HOPG electrode at the early stage of the reduction, could grow to the nanoplates rapidly, which dominantly constituted the dense Li_2O_2 film. The height of Li_2O_2 nanoplates was typically 5 nm, which was consistent with the step height of Li_2O_2 film. Upon oxidation, Li_2O_2 film was decomposed at the interface of Li_2O_2/HOPG electrode, and the thick insulating Li_2O_2 film delayed the complete decomposition due to its low electronic conductivity. All Li_2O_2 depleted without any notable remaining residue confirmed by AFM images and XPS analysis, which resulted in a reversible Li−O_2 reaction on the first cycle in the Li−O_2 model cell with ether-based electrolyte. However, byproducts such as Li_2CO_3, lithium acetate, and fluorine-related species manifested as nanoscaled particles and irregular forms after five cycles, which were caused by the deterioration of tetraglyme electrolyte, Li salt, and HOPG electrode. To achieve the reversible Li−O_2 reaction on cycling, which shows similar morphology of Li_2O_2 product after further reactions, new sets of Li−O_2 cells are needed. This research goal can be approached using the surface chemistry of carbon electrode surface, new catalysts for decomposition of byproduct, new electrolyte with high resistance to degradation by the superoxide radical, or new catalyst/electrode to enhance Li vacancies in Li_2O_2[6,45] or superoxide-dominant Li_2O_2.[46,47] We believe that the utilization of the EC-AFM imaging can promote the understanding of the total Li−O_2 reaction process in the improved cells, which can allow one to build strategies to prepare the optimum conditions for a Li−O_2 battery.

dx.doi.org/10.1021/ja405188g | J. Am. Chem. Soc. 2013, 135, 10870−10876

■ ASSOCIATED CONTENT

Supporting Information

Schematic view of Li−O_2 cell coupled with EC-AFM, Raman spectra, LSV, CVs, additional AFM images, and X-ray photoelectron spectra. This material is available free of charge via the Internet at http://pubs.acs.org.

■ AUTHOR INFORMATION

Corresponding Author

hrbyon@riken.jp

Notes

The authors declare no competing financial interest.

■ ACKNOWLEDGMENTS

This work was financially supported by RIKEN. M.H. is thankful for funding support from a short-term program for RIKEN International Program Associate (IPA). R.W. is thankful to the RIKEN RNC Industrial Cooperation Team for their support on XPS operation.

■ REFERENCES

(1) Girishkumar, G.; McCloskey, B.; Luntz, A. C.; Swanson, S.; Wilcke, W. *J. Phys. Chem. Lett.* **2010**, *1*, 2193.

(2) Bruce, P. G.; Freunberger, S. A.; Hardwick, L. J.; Tarascon, J.-M. *Nat. Mater.* **2012**, *11*, 19.

(3) Christensen, J.; Albertus, P.; Sanchez-Carrera, R. S.; Lohmann, T.; Kozinsky, B.; Liedtke, R.; Ahmed, J.; Kojic, A. *J. Electrochem. Soc.* **2012**, *159*, R1.

(4) Capsoni, D.; Bini, M.; Ferrari, S.; Quartarone, E.; Mustarelli, P. *J. Power Sources* **2012**, *220*, 253.

(5) Choi, N.-S.; Chen, Z.; Freunberger, S. A.; Ji, X.; Sun, Y.-K.; Amine, K.; Yushin, G.; Nazar, L. F.; Cho, J.; Bruce, P. G. *Angew. Chem., Int. Ed.* **2012**, *51*, 9994.

(6) Radin, M. D.; Rodriguez, J. F.; Tian, F.; Siegel, D. J. *J. Am. Chem. Soc.* **2011**, *134*, 1093.

(7) Viswanathan, V.; Nørskov, J. K.; Speidel, A.; Scheffler, R.; Gowda, S.; Luntz, A. C. *J. Phys. Chem. Lett.* **2013**, *4*, 556.

(8) Freunberger, S. A.; Chen, Y.; Peng, Z.; Griffin, J. M.; Hardwick, L. J.; Barde, F.; Novak, P.; Bruce, P. G. *J. Am. Chem. Soc.* **2011**, *133*, 8040.

(9) Freunberger, S. A.; Chen, Y.; Drewett, N. E.; Hardwick, L. J.; Barde, F.; Bruce, P. G. *Angew. Chem., Int. Ed.* **2011**, *50*, 8609.

(10) Chen, Y.; Freunberger, S. A.; Peng, Z.; Barde, F.; Bruce, P. G. *J. Am. Chem. Soc.* **2012**, *134*, 7952.

(11) Jung, H.-G.; Kim, H.-S.; Park, J.-B.; Oh, I.-H.; Hassoun, J.; Yoon, C. S.; Scrosati, B.; Sun, Y.-K. *Nano Lett.* **2012**, *12*, 4333.

(12) Younesi, R.; Urbonaite, S.; Edström, K.; Hahlin, M. *J. Phys. Chem. C* **2012**, *116*, 20673.

(13) Black, R.; Oh, S. H.; Lee, J.-H.; Yim, T.; Adams, B.; Nazar, L. F. *J. Am. Chem. Soc.* **2012**, *134*, 2902.

(14) Mitchell, R. R.; Gallant, B. M.; Thompson, C. V.; Shao-Horn, Y. *Energy Environ. Sci.* **2011**, *4*, 2952.

(15) Nanda, J.; Biheux, H.; Voisin, S.; Veith, G. M.; Archibald, R.; Walker, L.; Allu, S.; Dudney, N. J.; Pannala, S. *J. Phys. Chem. C* **2012**, *116*, 8401.

(16) Leskes, M.; Drewett, N. E.; Hardwick, L. J.; Bruce, P. G.; Goward, G. R.; Grey, C. P. *Angew. Chem., Int. Ed.* **2012**, *51*, 8560.

(17) Takechi, K.; Higashi, S.; Mizuno, F.; Nishikoori, H.; Iba, H.; Shiga, T. *ECS Electrochem. Lett.* **2012**, *1*, A27.

(18) Karan, N. K.; Balasubramanian, B.; Fister, T. T.; Burrell, A. K.; Du, P. *J. Phys. Chem. C* **2012**, *116*, 18132.

(19) Peng, Z.; Freunberger, S. A.; Hardwick, L. J.; Chen, Y.; Giordani, V.; Bardé, F.; Novák, P.; Graham, D.; Tarascon, J.-M.; Bruce, P. G. *Angew. Chem., Int. Ed.* **2011**, *50*, 6351.

(20) McCloskey, B. D.; Bethune, D. S.; Shelby, R. M.; Girishkumar, G.; Luntz, A. C. *J. Phys. Chem. Lett.* **2011**, *2*, 1161.

(21) McCloskey, B. D.; Scheffler, R.; Speidel, A.; Bethune, D. S.; Shelby, R. M.; Luntz, A. C. *J. Am. Chem. Soc.* **2011**, *133*, 18038.

(22) McCloskey, B. D.; Speidel, A.; Scheffler, R.; Miller, D. C.; Viswanathan, V.; Hummelshøj, J. S.; Nørskov, J. K.; Luntz, A. C. *J. Phys. Chem. Lett.* **2012**, *3*, 997.

(23) McCloskey, B. D.; Bethune, D. S.; Shelby, R. M.; Mori, T.; Scheffler, R.; Speidel, A.; Sherwood, M.; Luntz, A. C. *J. Phys. Chem. Lett.* **2012**, *3*, 3043.

(24) McCloskey, B. D.; Scheffler, R.; Speidel, A.; Girishkumar, G.; Luntz, A. C. *J. Phys. Chem. C* **2012**, *116*, 23897.

(25) Peng, Z.; Freunberger, S. A.; Chen, Y.; Bruce, P. G. *Science* **2012**, *337*, 563.

(26) Lu, Y.-C.; Crumlin, E. J.; Veith, G. M.; Harding, J. R.; Mutoro, E.; Baggetto, L.; Dudney, N. J.; Liu, Z.; Shao-Horn, Y. *Sci. Rep.* **2013**, *2*, 715.

(27) Lim, H.; Yilmaz, E.; Byon, H. R. *J. Phys. Chem. Lett.* **2012**, *3*, 3210.

(28) Laoire, C. O.; Mukerjee, S.; Abraham, K. M.; Plichta, E. J.; Hendrickson, M. A. *J. Phys. Chem. C* **2009**, *113*, 20127.

(29) Laoire, C. Ó.; Mukerjee, S.; Plichta, E. J.; Hendrickson, M. A.; Abraham, K. M. *J. Electrochem. Soc.* **2011**, *158*, A302.

(30) Herranz, J.; Garsuch, A.; Gasteiger, H. A. *J. Phys. Chem. C* **2012**, *116*, 19084.

(31) Lu, Y.-C.; Kwabi, D. G.; Yao, K. P. C.; Harding, J. R.; Zhou, J.; Zuin, L.; Shao-Horn, Y. *Energy Environ. Sci.* **2011**, *4*, 2999.

(32) Jung, H. G.; Hassoun, J.; Park, J. B.; Sun, Y. K.; Scrosati, B. *Nat. Chem.* **2012**, *4*, 579.

(33) Lu, Y.-C.; Gasteiger, H. A.; Crumlin, E.; McGuire, R.; Shao-Horn, Y. *J. Electrochem. Soc.* **2010**, *157*, A1016.

(34) Lu, Y.-C.; Gasteiger, H. A.; Shao-Horn, Y. *Electrochem. Solid-State Lett.* **2011**, *14*, A70.

(35) Lu, Y.-C.; Gasteiger, H. A.; Y, S.-H. *J. Am. Chem. Soc.* **2011**, *133*, 19048.

(36) Xiao, J.; Mei, D.; Li, X.; Xu, W.; Wang, D.; Graff, G. L.; Bennett, W. D.; Nie, Z.; Saraf, L. V.; Aksay, I. A.; Liu, J.; Zhang, J.-G. *Nano Lett.* **2011**, *11*, 5071.

(37) Wang, S.; Dong, S.; Wang, J.; Zhang, L.; Han, P.; Zhang, C.; Wang, X.; Zhang, K.; Lan, Z.; Cui, G. *J. Mater. Chem.* **2012**, *2*, 21051.

(38) Bowling, R. J.; Packard, R. T.; McCreery, R. L. *J. Am. Chem. Soc.* **1989**, *111*, 1217.

(39) Viswanathan, V.; Thygesen, K. S.; Hummelshoj, J. S.; Norskov, J. K.; Girishkumar, G.; McCloskey, B. D.; Luntz, A. C. *J. Chem. Phys.* **2011**, *135*, 214704.

(40) Ottakam Thotiyl, M. M.; Freunberger, S. A.; Peng, Z.; Bruce, P. G. *J. Am. Chem. Soc.* **2013**, *135*, 494.

(41) Gallant, B. M.; Mitchell, R. R.; Kwabi, D. G.; Zhou, J.; Zuin, L.; Thompson, C. V.; Shao-Horn, Y. *J. Phys. Chem. C* **2012**, *116*, 20800.

(42) Black, R.; Lee, J.-H.; Adams, B.; Mims, C. A.; Nazar, L. F. *Angew. Chem., Int. Ed.* **2013**, *52*, 392.

(43) Shao, Y.; Ding, F.; Xiao, J.; Zhang, J.; Xu, W.; Park, S.; Zhang, J.-G.; Wang, Y.; Liu, J. *Adv. Funct. Mater.* **2013**, *23*, 987.

(44) Lim, H.; Park, K.; Gwon, H.; Hong, J.; Kim, H.; Kang, K. *Chem. Commun.* **2012**, *48*, 8374.

(45) Hummelshoj, J. S.; Blomqvist, J.; Datta, S.; Vegge, T.; Rossmeisl, J.; Thygesen, K. S.; Luntz, A. C.; Jacobsen, K. W.; Nørskov, J. K. *J. Chem. Phys.* **2010**, *132*, 071101.

(46) Mo, Y.; Ong, S. P.; Ceder, G. *Phys. Rev. B* **2011**, *84*, 205446.

(47) Gerbig, O.; Merkle, R.; Maier, J. *Adv. Mater.* **2013**, *25*, 3129.